

# Dissolvable Metals for Transient Electronics

Lan Yin, Huanyu Cheng, Shimin Mao, Richard Haasch, Yuhao Liu, Xu Xie, Suk-Won Hwang, Harshvardhan Jain, Seung-Kyun Kang, Yewang Su, Rui Li, Yonggang Huang, and John A. Rogers\*

**Reactive dissolution and its effects on electrical conduction, morphological change and chemical transformation in thin films of Mg, AZ31B Mg alloy, Zn, Fe, W, and Mo in de-ionized (DI) water and simulated body fluids (Hanks' solution pH 5–8) are systematically studied, to assess the potential for use of these metals in water-soluble, that is, physically "transient", electronics. The results indicate that the electrical dissolution rates in thin films can be much different than traditionally reported corrosion rates in corresponding bulk materials. Silicon metal oxide field effect transistors (MOSFETs) built with these metals demonstrate feasibility for use in transient electronics.**

## 1. Introduction

Transient electronics represents an emerging class of technology whose key characteristic is that it physically disappears, in whole or in part, in a controlled fashion after it has served its targeted function.<sup>[1–5]</sup> Devices with this property provide capabilities that complement those of traditional integrated circuits. Enabled applications range from biodegradable electronic medical implants, secure electronics, to vanishing environmental sensors, and zero-waste consumer electronics.<sup>[1]</sup> Here, the constituent materials must be carefully formulated and

integrated together to accommodate a desired transient process, such as dissolution in biofluids or ground water. Silicon, which undergoes hydrolysis in basic aqueous conditions, is an attractive choice for the semiconductor.<sup>[1]</sup> Zinc oxide<sup>[2]</sup> and certain organic semiconductors<sup>[5]</sup> represent alternatives. In all cases, compatible conductive materials are also essential. By comparison to conductive polymers, conventional metals are appealing due to their low resistivities, stable properties, and established roles in commercial devices. Initial reports of silicon transient

electronics used magnesium (Mg) for electrodes and interconnects,<sup>[1]</sup> due to its combination of ease in processing, rapid rates of hydrolysis, and biocompatibility. Alternative metals that share some of these characteristics include zinc (Zn), iron (Fe), tungsten (W), and molybdenum (Mo). Each of these materials, with the exception of W (not a universal bioelement),<sup>[6]</sup> is essential for biological function, with recommended daily intake values in the range of  $\approx 0.05$ – $400 \text{ mg day}^{-1}$ .<sup>[7,8]</sup> In addition, Mg, Mg alloys, and Fe have been explored for use in bioresorbable implants (e.g., vascular stents) due to their biocompatibility and favorable mechanical properties.<sup>[9–12]</sup> In simulated body fluids (SBFs) and at physiological conditions, Mg dissolves to form mainly  $\text{Mg}(\text{OH})_2$  which is water soluble, at a rate  $\approx 0.05$ – $0.5 \mu\text{m h}^{-1}$ .<sup>[13–16]</sup> Addition of small amounts of aluminum (3 wt%–9 wt%) can slow these rates to  $\approx 0.02$ – $0.10 \mu\text{m h}^{-1}$ .<sup>[14,15,17]</sup> In related conditions, Fe dissolves to form hydroxides ( $\text{Fe}(\text{OH})_2$  or/and  $\text{Fe}(\text{OH})_3$ ) and oxides ( $\text{Fe}_2\text{O}_3$ ,  $\text{Fe}_3\text{O}_4$  or/and  $\text{FeO}$ ) at  $\approx 0.02 \mu\text{m h}^{-1}$ ,<sup>[18–21]</sup> with rates that can be significantly slower in Fe stents evaluated in vivo.<sup>[22]</sup> In contrast to Mg, Fe degrades in a spatially non-uniform manner, with certain reaction products ( $\text{Fe}_2\text{O}_3$  and  $\text{Fe}_3\text{O}_4$ ) that have very low solubility.<sup>[9,23]</sup> Bowen et al. recently suggested the use of Zn as an alternative metal for the resorbable stents,<sup>[24]</sup> due to its acceptable in vivo degradation rates ( $\approx 5 \times 10^{-3} \mu\text{m h}^{-1}$ ) and soluble dissolution products  $\text{ZnO}$ .<sup>[25]</sup>

Metals with less comprehensive data on biocompatibility are also worthy of consideration. For example, published results suggest that W can dissolve in physiological solutions to  $\text{WO}_x$  and Mo can degrade in neutral buffer solutions to  $\text{MoO}_x$ .<sup>[26–28]</sup> Neural sensor wires made of W dissolve at rates of  $\approx 0.02$ – $0.06 \mu\text{m h}^{-1}$  in SBF at room temperature (RT).<sup>[26]</sup> In vivo tests of W embolisation coils indicate no obvious adverse biological effects, with minimal toxicity for concentrations  $< 50 \mu\text{g mL}^{-1}$ .<sup>[29,30]</sup> Although in vivo dissolution of pure Mo has not been reported, the rates in pH 7 buffer and NaCl solutions

Dr. L. Yin, S. Mao, Dr. R. Haasch, Y. Liu, X. Xie, S.-W. Hwang, Dr. S.-K. Kang, Prof. J. A. Rogers  
Department of Materials Science and Engineering  
Beckman Institute for Advanced Science and Technology  
and Frederick Seitz Materials Research Laboratory  
University of Illinois at Urbana-Champaign  
Urbana, IL, 61801, USA  
E-mail: jrogers@illinois.edu



H. Cheng, Dr. Y. Su, Prof. Y. Huang  
Department of Mechanical Engineering and Department  
of Civil and Environmental Engineering  
Northwestern University

Center for Engineering and Health  
and Skin Disease Research Center  
Evanston, Illinois, 60208, USA

H. Jain  
Department of Electrical and Computer Engineering  
University of Illinois at Urbana-Champaign  
Urbana, IL, 61801, USA

Dr. R. Li  
State Key Laboratory of Structural Analysis for Industrial Equipment  
Department of Engineering Mechanics  
Dalian University of Technology  
Dalian, 116024, China

DOI: 10.1002/adfm.201301847

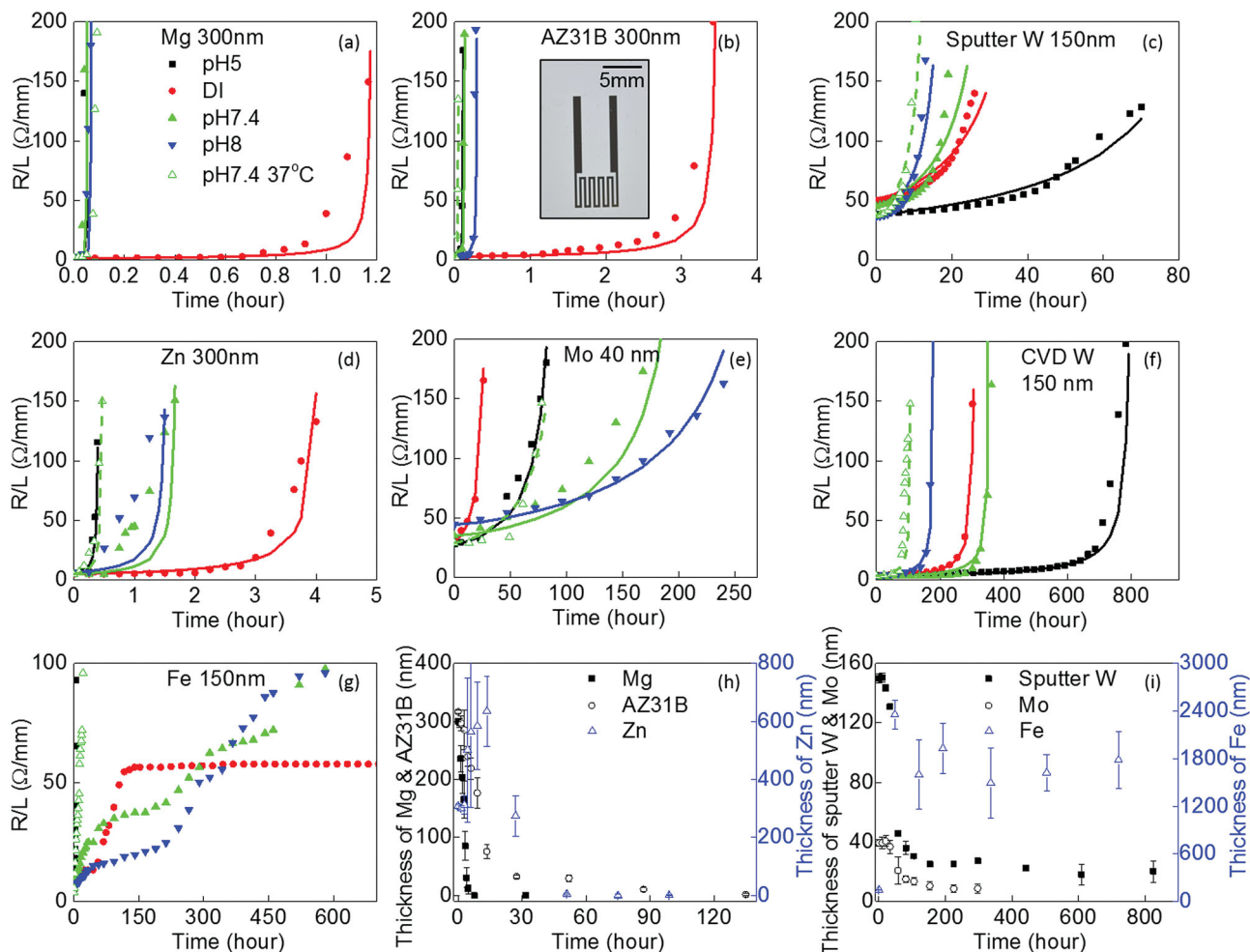


**Figure 1.** Change in resistance of serpentine thin film traces as a function of time during dissolution in Hanks' solution (pH 5, 7.4 and 8 at RT and pH 7.4 at 37 °C) and in DI water, for cases of a) Mg (300 nm); b) AZ31B Mg alloy (300 nm); c) sputter deposited W (150 nm); d) Zn (300 nm); e) Mo (40 nm); f) CVD W (150 nm); g) Fe (150 nm); a–g) share the same legend. Change in thickness of similar traces as a function of time during dissolution in DI water at RT for cases of h) Mg, AZ31B Mg alloy, and Zn; i) Mo, Fe and sputter deposited W.

are between  $\approx 10^{-4}$  and  $10^{-3} \mu\text{m h}^{-1}$  at RT.<sup>[27,31]</sup> Such low rates can be important for classes of devices that demand sustained, continuous contact between electrodes and internal tissues.

These considerations suggest that Mg, Mo, W, Fe, and Zn are promising candidates for additional study as patterned, thin film traces in transient electronic implants, environmental monitors and others. Although there is an extensive, existing body of knowledge related to corrosion of these metals in bulk form, far less information is available for thin films, where behaviors can be quite different. For example, the grain sizes in films and bulk samples typically lie in qualitatively distinct regimes, with significant consequences.<sup>[32]</sup> Furthermore, pinholes, pitting, porosity, and other phenomena have dominating effects on specific properties relevant to use of thin films in transient electronics, particularly in time dependent variations of the resistances of patterned traces. The following outlines systematic studies of dissolution behaviors, in terms of electrical conductivity, thickness, morphology, and surface chemistry, of Mg, AZ31B (3 wt% Al and 1 wt% Zn) Mg alloy, Zn,

Fe, W, and Mo thin films and serpentine wires in de-ionized (DI) water and simulated body fluids (Hanks' solution). Silicon metal oxide field effect transistors (MOSFETs) built using electrodes formed with these various metals demonstrate their utility in transient electronics.

## 2. Results and Discussion

### 2.1. Kinetics Determined by Changes in Electrical Properties

**Figure 1a–g** summarizes representative dissolution behavior in terms of the change in resistance as a function of time for various metal thin films in DI water and Hanks' solutions (for pH values between 5 and 8) at both RT and body temperature (37 °C). The geometry of the serpentine traces (width 250  $\mu\text{m}$ ; total length  $\approx 50$  mm) used for evaluations is illustrated in Figure 1b, including the top probing pads. The change in resistance shown in Figure 1 is normalized by the total length of the

**Table 1.** Summary of dissolution rates of various metals and comparison with literature data.

	Electrical dissolution rates [ $\mu\text{m h}^{-1}$ ]		Apparent morphological dissolution rates in DI water [ $\mu\text{m h}^{-1}$ ]	Mass lost corrosion rates from literature [ $\mu\text{m h}^{-1}$ ]	Refs.
	DI	Hanks' solutions			
Mg	$0.3 \pm 0.1$	$4.8 \pm 2.2$	$\approx 0.07$	pH 7.4 SBF 37 °C: 0.05–0.5 0.05 m NaCl: 0.05–0.3	[13–16] [47]
AZ31B	$0.08 \pm 0.02$	$2.6 \pm 2.1$	$\approx 0.02$	pH 7.4 SBF 37 °C: 0.02–0.1 0.05 m NaCl: $\approx 0.3$ 0.6 m NaCl: $\approx 0.1$	[14,15,17] [47] [48]
W (S) <sup>a)</sup>	$(4 \pm 1) \times 10^{-3}$	pH 5: $(1.4 \pm 0.4) \times 10^{-3}$ pH 7.4–8: $(8 \pm 2) \times 10^{-3}$ pH 7.4 37 °C: $\approx 0.02$	$\approx 1.7 \times 10^{-3}$	pH 7.4 SBF: 0.02–0.06	[26]
W (C) <sup>a)</sup>	$(7 \pm 2) \times 10^{-4}$	pH 5: $\approx 2 \times 10^{-4}$ pH 7.4–8: $(7 \pm 2) \times 10^{-4}$ pH 7.4 37 °C: $\approx 2 \times 10^{-3}$	$\approx 3 \times 10^{-4}$		
Mo	$(1 \pm 0.1) \times 10^{-3}$	pH 5: $(6 \pm 2) \times 10^{-4}$ pH 7.4–8: $(2 \pm 0.3) \times 10^{-4}$ pH 7.4 37 °C: $(7 \pm 4) \times 10^{-4}$	$\approx 3 \times 10^{-4}$	pH 7 buffer: $1 \times 10^{-3}$ pH 7 buffer thin film: $2 \times 10^{-4}$	[27] [31]
Zn	$0.07 \pm 0.02$	$0.3 \pm 0.2$	$\approx 7 \times 10^{-3}$	In vivo: $\approx 5 \times 10^{-3}$ DI water: $\approx 3 \times 10^{-3}$ Sea water: $\approx (2-8) \times 10^{-3}$	[24] [35] [35]
Fe	$< 1 \times 10^{-3}$	pH 5: $\approx 9 \times 10^{-3}$ pH 7.4–8: $\approx 2 \times 10^{-4}$ pH 7.4 37 °C: $\approx 7 \times 10^{-3}$	-	pH 7.4 SBF 37 °C: $\approx 0.02$	[18,19]

<sup>a)</sup>W(S) and W(C) stand for sputter deposited W and CVD W, respectively. All the data are at RT unless specified.

serpentine pattern. Changes in thickness with time for dissolution in DI water at RT appear in Figure 1h,i. In all cases, an ultrathin layer of Cr ( $\approx 10$  nm) serves as an adhesion promoter to a glass substrate. This layer improves the yields and ensures that the dissolution kinetics are not interrupted by film delamination. (Control experiments without the Cr establish that, in the absence of delamination, this layer has no measurable effect on the dissolution processes.)

For purposes of discussion, electrical dissolution rates (EDR) are defined by converting changes in electrical resistance to an effective (non-physical) thickness  $h$ , according to  $R = R_0 h_0 / h$  (with  $R_0$  and  $h_0$  the initial electric resistance and initial thickness respectively), and using results of a reactive diffusion model discussed subsequently. Results, each of which corresponds to the average of at least three data sets, appear in Table 1. For Fe, whose behavior is not captured by the model, the EDR is estimated by dividing the Fe thickness (150 nm) over the time required for complete loss in conductivity ( $R/L > 100 \Omega \text{ mm}^{-1}$ ). Overall, i) Mg, AZ31B Mg alloy and Zn have EDRs that are much higher than those of W, Mo, and Fe; ii) the EDRs of Mg, Mg alloy, and Zn increase in salt solutions; iii) the EDRs increase with body temperature (between RT and 37 °C) for W, Mo, and Fe, but not significantly for Mg, AZ31B Mg alloy, and Zn. The detailed dissolution chemistries that underlie these behaviors are discussed in Section 2.2.

As shown in Figure 1a,b and Table 1, in DI water, the EDR of AZ31B Mg alloy is approximately three times lower than that of Mg. In both cases,  $\text{Mg}(\text{OH})_2$  is the main dissolution product, as discussed subsequently. The EDRs of both Mg and Mg alloy are significantly higher ( $> 10$  times) in Hanks' solution regardless of pH and temperature (for the ranges studied), likely due to the presence of chlorides ( $\text{Cl}^-$ ) that promote rapid attack, as reported in corrosion studies of mass loss in bulk samples of Mg.<sup>[33]</sup> The weak dependence on pH between 5 and 8 is consistent with findings for bulk Mg alloys in NaCl solutions.<sup>[34]</sup> On the other hand, a much stronger influence of pH was reported for bulk samples in Hanks' solutions, with dissolution rates  $\approx 300$  times faster in pH 5.5 compared to the pH 8 solutions.<sup>[16]</sup>

In a trend qualitatively similar to that for Mg, Zn shows an EDR that is approximately four times lower in DI water than in salt solution, possibly due to the presence of chlorides ( $\text{Cl}^-$ ).<sup>[35]</sup> As will be discussed later, the dissolution products are mainly ZnO and  $\text{Zn}(\text{OH})_2$ . The EDRs among salt solutions with different pH values and temperatures are similar, which is consistent with mass loss associated with corrosion of bulk Zn in NaCl solutions.<sup>[35]</sup>

Unlike Mg and Zn, Mo (Figure 1e and Table 1) exhibits EDRs in DI water that are higher ( $\approx 2-5$  times) than those in salt solutions at RT, with Mo oxides as corrosion products. Such trends are observed in bulk Mo materials.<sup>[36]</sup> The differences likely arise

from the strong dependence of Mo dissolution on oxygen solubility in aqueous solution, with rates that increase with oxygen solubility (Corrosion rates increase  $\approx 4$  times with oxygen from 9 ppm to 37 ppm in DI water).<sup>[37]</sup> The presence of ions (e.g.,  $\text{Na}^+$ ,  $\text{Cl}^-$ ),<sup>[36,38]</sup> is known to reduce oxygen solubility. This effect, in Mo, could counteract any increase in corrosion potential associated with chlorides. As illustrated in Figure 1e and Table 1, Mo has an EDR that is  $\approx 3$  times lower in solutions with pH of 7.4 and 8 compared to pH 5. Although dissolution rates of thin films of Mo are roughly 10 times higher in strong alkaline solution (pH 12) compared to neutral (pH 7) or acidic solutions (pH 2),<sup>[31]</sup> the expected reductions in oxygen solubility with increasing basicity can again surpass the effects of pH in this range.<sup>[36,38]</sup> In addition, the EDR for Mo is approximately three times higher at 37 °C than at RT, for Hanks' solution at pH 7.4.

W exhibits an EDR that is four times lower in acidic salt solution (pH 5) compared to more basic solutions (pH 7.4–8), as shown in Figure 1c and Table 1. Here, W oxides are the dissolution products. The trend is qualitatively consistent with the corrosion behavior of bulk W materials.<sup>[28]</sup> The EDR of W in DI water is similar to that in solutions with pH 7.4–8. Elevated temperatures (37 °C) increase the EDR. By comparison to the other metals, the EDR for W is more sensitive to deposition conditions. An example appears in Figure 1c,f and Table 1, where W formed by chemical vapor deposition (CVD) has an EDR about 10 times lower compared to the value for sputtered W. The dependence on pH for these two cases is qualitatively similar. The quality of sputter deposited thin films of W can be adjusted through sputtering power, argon pressure and vacuum level (Figure S1, Supporting Information).

As given in Figure 1g and Table 1, the EDR for Fe is highest for pH 5 solution (acidic solution) and for pH 7.4 at 37 °C (elevated temperature), while lower in the other cases. For all examined conditions, thick layers of iron oxides form on the surfaces. Furthermore, the resistance as a function of time shows plateaus, especially for Fe in DI water, where the dissolution apparently ceases after 120 h. Such phenomena likely result from the overall slow kinetics and the protective nature of iron oxides, as discussed subsequently.

Corresponding changes in thickness during dissolution in DI water appear in Figure 1h,i. The apparent morphological dissolution rates extracted by linear fitting of the initial stages of thickness changes upon dissolution enable quantitative comparisons to the EDRs. (The later stages of dissolution involve significant contributions due to porosity, non-uniformities and residual oxides). For Zn and Fe, the oxides can result in increases in thickness with time. Here, the averaged morphological dissolution rate of Zn is defined simply as the initial thickness 300 nm divided by the time for complete dissolution. Rates of change in thickness for Fe cannot be determined accurately because the measured thickness does not vary significantly over the course of observation for one month. The results, which appear in Table 1, show that the decrease in thickness lags the increase in resistance, mainly due to i) contribution of residual insulating oxides to the measured thickness, especially for the case of Zn; ii) enhanced sensitivity of resistance to local non-uniformities, pinholes and porosity. The most relevant parameter for transient electronics is, of course, the resistance; thickness is not an adequate substitute. For

example, as shown in Figure 1h,i, the thicknesses of films of Mg, Mg alloy, and Zn reach zero after the complete loss in electrical continuity. For W and Mo, the thickness decreases quickly in the first 4 days, after which the oxide products slowly dissolve. In the case of Fe, the oxides do not dissolve even over the course of a month. Such retention of Fe corrosion products also occurs in *in vivo* tests of Fe stents.<sup>[9]</sup>

The corrosion rates, defined by mass loss for bulk materials in near neutral solutions as reported in literature, are also summarized in Table 1. The EDRs of Mg, Mg alloys, and Zn thin films are higher ( $\geq 10$  times) than the corrosion rates under similar conditions; Mo exhibits similar rates; and W and Fe show EDRs that are lower ( $\approx 3$ –30 times depending on the conditions). At least two considerations are important in understanding these differences. First, the films consist of nanocrystallines (grain size  $\approx 10$ –60 nm) that can improve corrosion resistance compared to bulk materials with much larger grain size,<sup>[32]</sup> possibly due to the formation of surface oxides with enhanced protective qualities on the nano-grained surfaces.<sup>[39]</sup> Previous results of corrosion studies on Mg, Fe, Zn, W, and Mo nanocrystalline films suggest that the dissolution rates can decrease by  $\approx 2$ –10 times with decreasing grain size.<sup>[18,31,39–42]</sup> By contrast, Mg alloy shows little effect of grain size.<sup>[43]</sup> Second, and perhaps most important, the resistances of thin films are sensitive to non-uniformities, as mentioned previously. One consequence is that when such non-uniformities (either at large or small scales) are important, the EDR is larger than the reported corrosion rates, as for Mg, Mg alloys, and Zn, as discussed subsequently. On the other hand, if grain size effects are pronounced, then the EDR can be strongly reduced, as for W and Fe. When the influence of non-uniformities and grain sizes are similar, then the EDR can be comparable to the reported rates, as for Mo. The conclusion, then, is that thickness changes and corrosion rates can be important, but they are both distinct and often times significantly different than EDRs, as they relate to uses of thin films in transient electronics.

In spite of these differences, we find that simple models of reactive diffusion that connect thickness directly to resistance are capable of capturing the trends. An analytical model of reactive diffusion<sup>[44]</sup> is designed to describe the dissolution behavior in terms of electrical conductivity, as shown in the solid lines of Figure 1. The model reproduces the observed behavior in all cases except for Fe, for reasons highlighted previously. Resistance changes are represented by changes in an effective thickness ( $h$ ) that accounts, in an approximate manner, both for changes in physical thickness and for influences associated with porosity, pitting and other non-uniformities, as described previously in this section. The model considers both chemical reactions at the water/metal interfaces and diffusion of water into the metal. The key parameters are the diffusivity of water in the metal film,  $D$ , and the reaction rate constant  $k$ . Because  $h_0$  is much smaller than the lengths and widths of the patterned traces, a 1D model can capture the behaviors. With  $z = 0$  at the bottom surface of the metal, the water concentration  $w$  at time  $t$  satisfies the reactive diffusion equation:

$$D\partial^2 w / \partial z^2 - kw = \partial w / \partial t \quad (1)$$

For a constant water concentration at the top surface of the metal  $w|_{z=h_0} = w_0$  ( $w_0 = 1 \text{ g cm}^{-3}$ ) and zero water flux

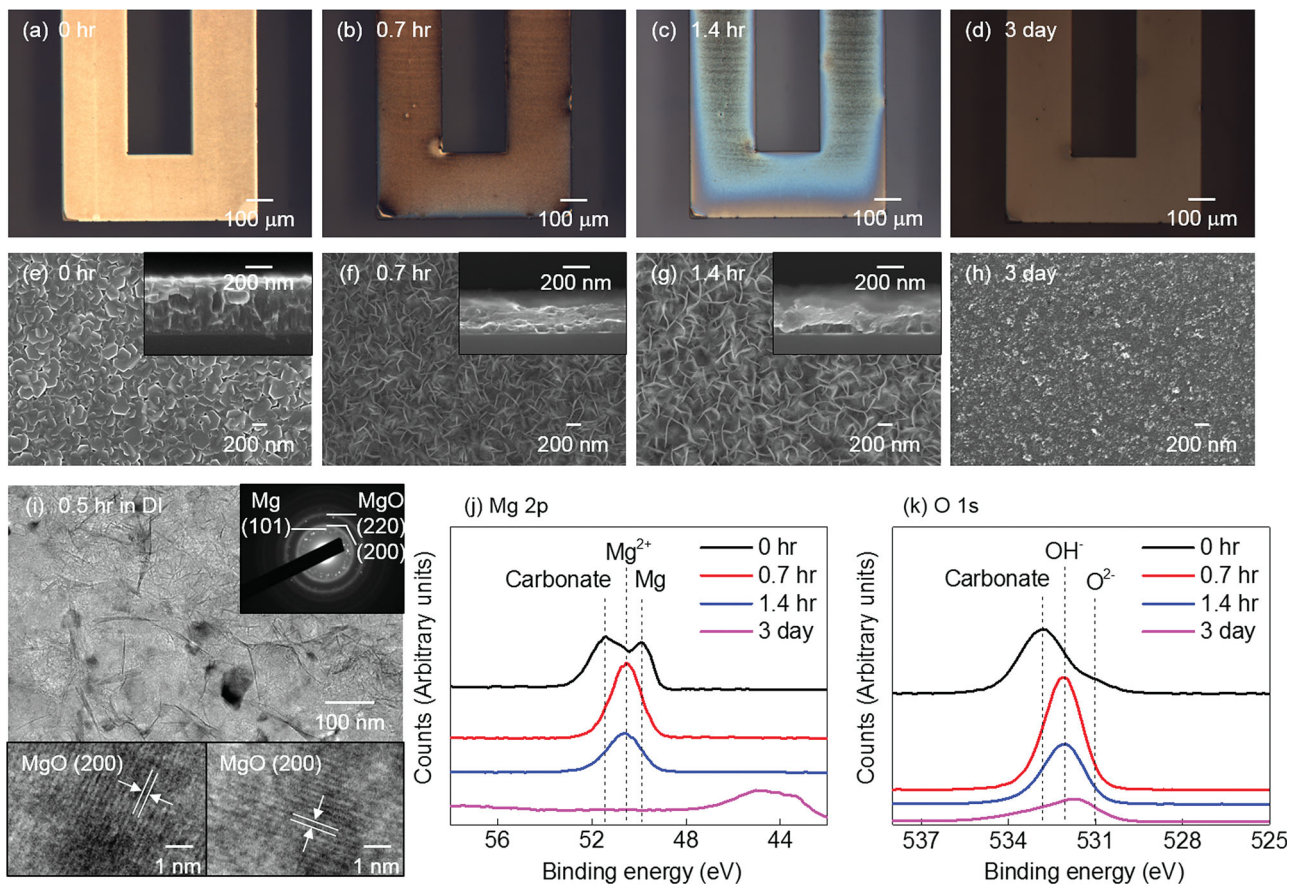


**Figure 2.** Evolution of microstructure and surface chemistry associated with dissolution of Mg in DI water. a–d) optical images; e–h) SEM images with cross-sectional views in the insets; i) TEM bright field image with diffraction patterns and lattice fringes; j,k) XPS data.

$\partial w / \partial t|_{z=0} = 0$  at the bottom surfaces, Equation 1 can be solved by the method of separation of variables. By considering that one mole of metal reacts with  $q$  moles of water, the integration of metal dissolved at each location through the thickness of the film and over time gives the remaining thickness of metal thin films, normalized by its initial thickness  $h_0$  as

$$\frac{h}{h_0} \approx 1 - \frac{t}{t_c} \quad (2)$$

where  $t_c = h_0 q \rho M_{H_2O} (\sqrt{k D w_0 M})^{-1} \tanh^{-1} \sqrt{k h_0^2 / D}$  is the critical time when the thickness reaches zero,  $\rho$  is the mass density of metal,  $M$  and  $M_{H_2O}$  are the molar masses of metal and water, respectively. The EDR can therefore be estimated according to:

$$v_{EDR} = -\frac{dh}{dt} = \sqrt{k D} \frac{w_0 M}{q \rho M_{H_2O}} \tanh \sqrt{\frac{k h_0^2}{D}} \quad (3)$$

Two free parameters,  $D$  and  $k$ , are allowed to vary to yield good fits to the measured resistance curves in Figure 1a–f, where the diffusivity  $D$  is constrained to a reasonable range ( $\approx 10^{-10}$ – $10^{-17}$  cm<sup>2</sup> s<sup>−1</sup>), with reference to diffusivities of water in sputtered silica at RT ( $\approx 10^{-11}$  cm<sup>2</sup> s<sup>−1</sup>)<sup>[45]</sup> and silica glass ( $\approx 10^{-16}$  cm<sup>2</sup> s<sup>−1</sup>)<sup>[46]</sup> since values for the diffusivity of water in metal thin films are not generally available in the literature. The following diffusivities are obtained,  $D = 6 \times 10^{-12}$  cm<sup>2</sup> s<sup>−1</sup> at RT and  $D = 1.2 \times 10^{-11}$  cm<sup>2</sup> s<sup>−1</sup> at 37 °C for Mg, Mg alloys, and

Zn, and  $D = 1 \times 10^{-16}$  cm<sup>2</sup> s<sup>−1</sup> at RT and  $D = 2 \times 10^{-16}$  cm<sup>2</sup> s<sup>−1</sup> at 37 °C for W and Mo. Equation 3 can be therefore used to estimate the EDRs, where  $q$  is 2 for Mg, Mg alloy, and Zn ( $Mg + 2H_2O \rightarrow Mg(OH)_2 + H_2$ ,  $Zn + 2H_2O \rightarrow Zn(OH)_2 + H_2$ ); and 1 for Mo and W ( $2Mo + 2H_2O + 3O_2 \rightarrow 2H_2MoO_4$ ,  $2W + 2H_2O + 3O_2 \rightarrow 2H_2WO_4$ ). The results are summarized in Table 1.

## 2.2. Microstructure and Surface Chemistry Associated with Reactive Dissolution

Detailed investigations involving metal films in DI water establish the basic mechanisms and effects. In all cases, i) mass loss occurs at rates lower than the EDR, due primarily to the formation of micropores and/or pits; ii) oxides as dissolution products appear on the surfaces, where they can act as partially protective layers to slow the dissolution of underlying metal; iii) the residual oxide layers dissolve much more slowly than the metal.

### 2.2.1. Mg and AZ31B Mg Alloy

The evolution of microstructure and surface chemistry during the course of dissolution in DI water for Mg and Mg alloy appear in Figures 2,3 respectively. At a macroscopic scale, dissolution is uniform for both Mg and AZ31B Mg alloy

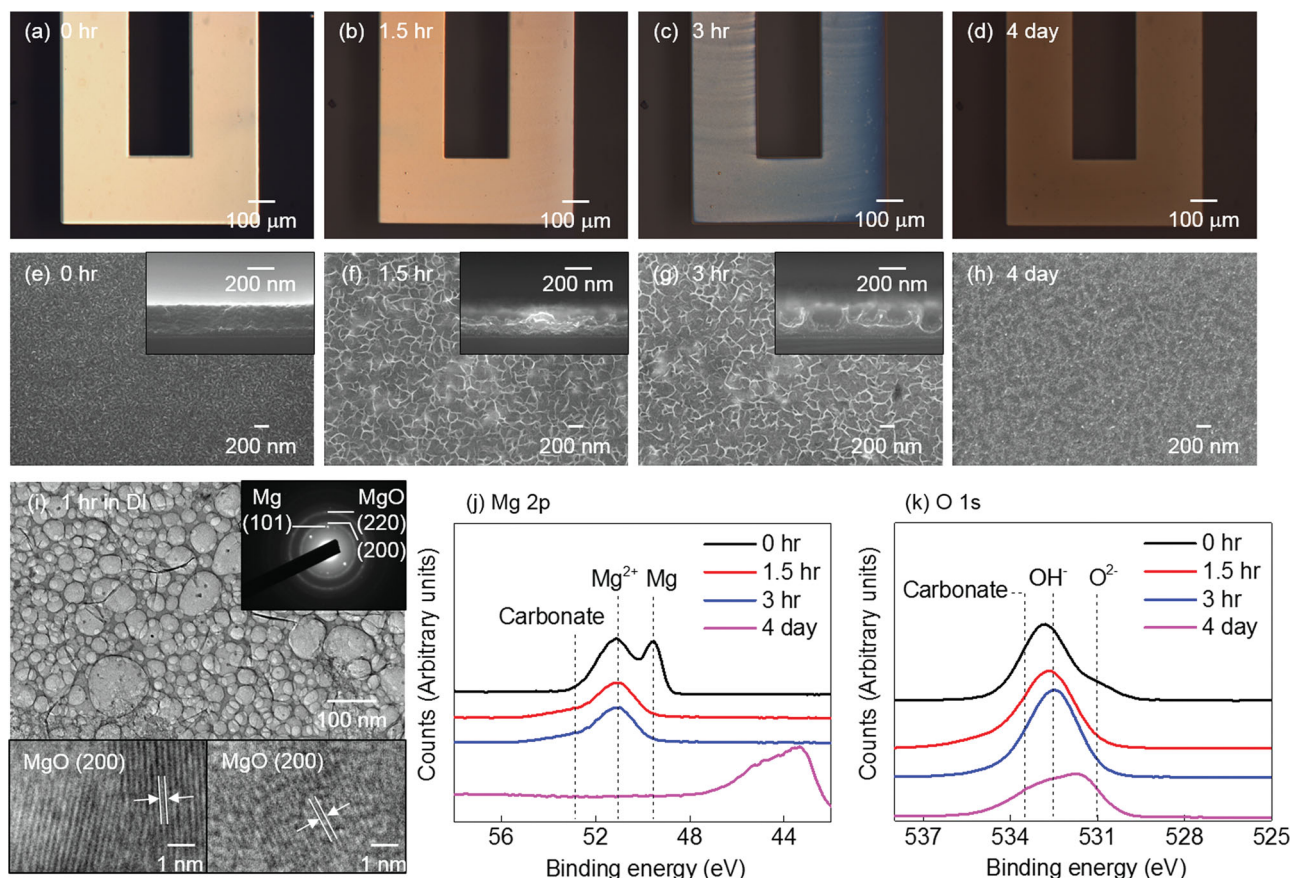


**Figure 3.** Evolution of microstructure and surface chemistry associated with dissolution of AZ31B Mg alloy in DI water. a–d) optical images; e–h) SEM images with cross-sectional views in the insets; i) TEM bright field image with diffraction patterns and lattice fringes; j–k) XPS data.

(Figures 2, 3a–d). Micropores develop and the surface roughens and becomes uneven as dissolution proceeds (Figures 2, 3f,g). Needle-like dissolution products appear (Figures 2, 3f,g), consistent with previous reports of bulk Mg and AZ31B alloy samples in simulated bio-fluids.<sup>[49,50]</sup> Figures 2, 3j,k present X-ray photoelectron spectroscopy (XPS) results with peak identifications referenced to data by Liu et al.<sup>[51]</sup> The assigned binding energies are Mg (49.9 eV), Mg(OH) (50.5 eV), and carbonate (51.5 eV) for Mg 2p; and Mg–O (531.0 eV), Mg–OH (532.1 eV), and carbonate (532.8 eV) for O 1s. The binding energies for AZ31B Mg alloy are Mg (49.5 eV), Mg(OH) (51.0 eV), and carbonate (52.8 eV) for Mg 2p; and Mg–O (531.0 eV), Mg–OH (532.5 eV), and carbonate (533.5 eV) for O 1s. The increases in binding energies for hydroxyls and carbonates likely arise from the presence of Al.<sup>[51]</sup> Surface oxides/hydroxide/carbonates can be found on the film, even before immersion, due to the presence of oxygen, water vapor and carbon dioxide in the atmosphere. During dissolution, the outer surface consists mainly of Mg(OH)<sub>2</sub>, possibly with a small amount of MgO and carbonates (Figures 2, 3j,k), as reported previously with bulk samples.<sup>[51,52]</sup> The layer of Mg(OH)<sub>2</sub> is estimated to have a thickness greater than 10 nm, based on the probing depth of the XPS technique and the absence of metallic Mg peaks. As reported by other researchers,<sup>[53–55]</sup> Mg(OH)<sub>2</sub> is a major surface product of Mg corrosion in common biological solutions. The

presence of Na<sup>+</sup>, Cl<sup>−</sup>, PO<sub>4</sub><sup>3−</sup>, and CO<sub>3</sub><sup>2−</sup> in these solutions can introduce phosphates and carbonates into the surface layer. The transmission electron microscopy (TEM) bright field images (Figures 2, 3i) illustrate metallic Mg and needle-like oxide products, consistent with the scanning electron microscopy (SEM) images. The TEM diffraction patterns and lattice fringes indicate the presence of crystalline MgO, suggesting a possible amorphous nature of the outer Mg(OH)<sub>2</sub> layer.<sup>[56]</sup> These results are consistent with the proposed bi-layer surface oxide structure of bulk Mg dissolved in water or NaCl solution, with a thick outer layer rich in Mg(OH)<sub>2</sub> on top of a thin crystalline MgO film.<sup>[54,56]</sup> The MgO likely forms immediately after exposure of fresh metallic surface to oxygen in the atmosphere. The Mg(OH)<sub>2</sub> layer increases in thickness as the dissolution proceeds, due to hydration of the native MgO followed by a dissolution-precipitation mechanism at the expense of base metal.<sup>[56]</sup> As shown previously in Table 1, the EDR is approximately four times faster than the rate of change in thickness for both Mg and Mg alloy. In particular, 300 nm thick films of Mg and AZ31B Mg alloy become electrically discontinuous in ≈1.5 and ≈3 h, respectively, as shown in Figure 1a,b. The results of Figures 2, 3c,g suggest, however, that some base metal still exists at this stage. As time proceeds, the remaining metal reacts to leave only residual Mg(OH)<sub>2</sub> and MgO. Because of the relatively high solubility of Mg(OH)<sub>2</sub> and MgO in water,<sup>[57]</sup> the

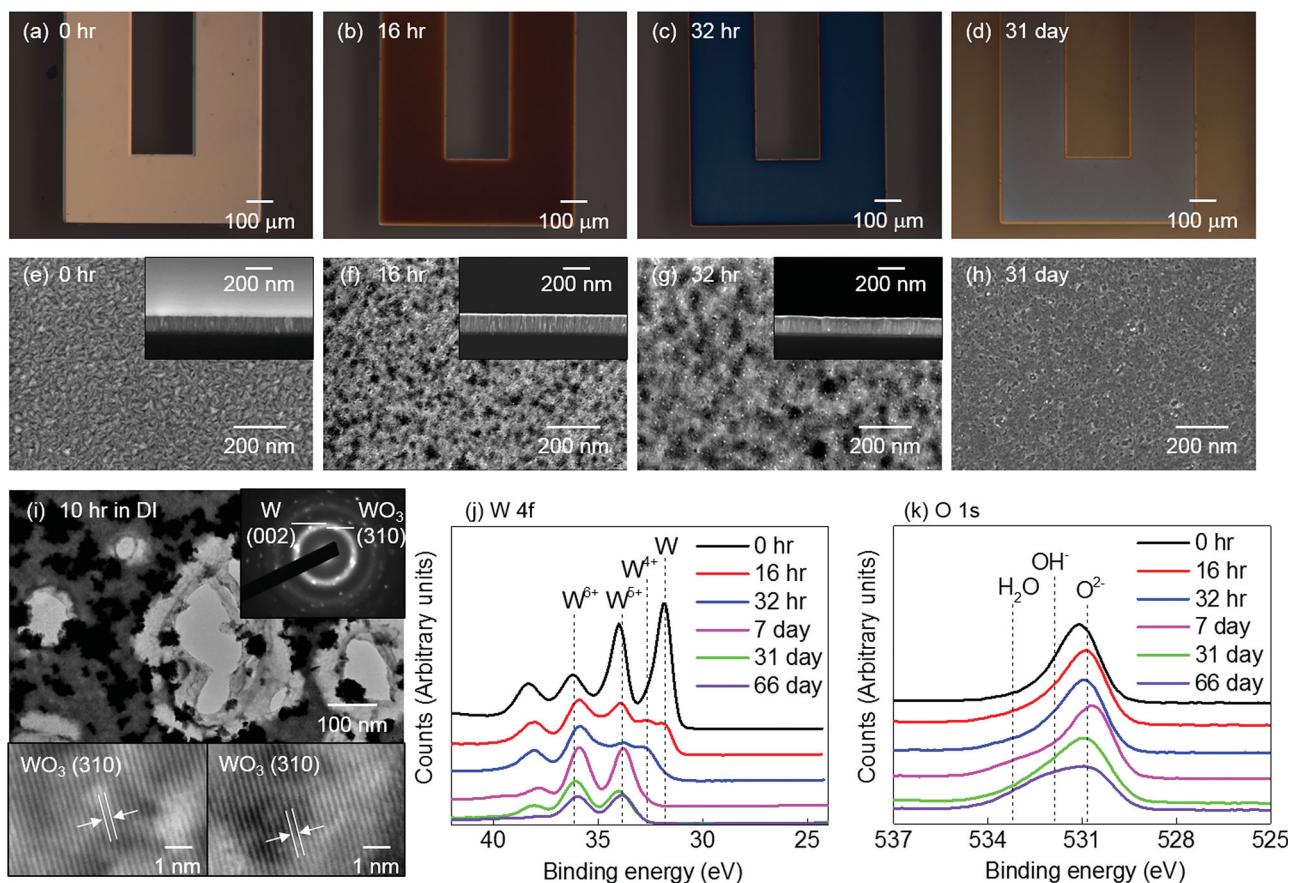


**Figure 4.** Evolution of microstructure and surface chemistry associated with dissolution of sputtered deposited W in DI water. a–d) optical images; e–h) SEM images with cross-sectional views in the insets; i) TEM bright field image with diffraction patterns and lattice fringes; j,k) XPS data.

oxides eventually disappear completely after 1–4 days, leaving only the Cr adhesion layer, as confirmed by the XPS data (Figures 2,3d,h,j,k). The dissolution rates of Mg oxides/hydroxides are estimated to be  $\approx 5\text{--}8\text{ nm day}^{-1}$ , determined from fits of the later stages of dissolution in Figure 1h.

### 2.2.2. W and Mo

Results for dissolution of sputter deposited W and Mo in DI water appear in **Figures 4, 5**. As transition metals in the same column of the periodic table, W and Mo are expected to have similar surface chemistry. As can be seen, the surface morphologies of W and Mo during dissolution are mostly uniform based on the optical observations (Figures 4,5a–d). Micropores are evident, however, in SEM results (Figures 4,5f,g) and more clearly in the TEM bright field images (Figures 4,5i).

XPS analysis reveals that the W film has an initial native oxide, mostly  $\text{WO}_3$  (Figure 4j,k). As dissolution proceeds, a mixture of oxides ( $\text{W}^{4+}$ ,  $\text{W}^{5+}$ , and  $\text{W}^{6+}$ ) develops at the surface. The thickness of these oxides increases to values larger than 10 nm after  $\approx 32\text{ h}$ , as inferred by disappearance of the metallic W signal in the XPS data. Further reaction eliminates the  $\text{W}^{4+}$  and  $\text{W}^{6+}$  oxides, leaving only the  $\text{W}^{5+}$  oxide (Figure 4j,k). The oxygen peaks of W in Figure 4k suggest the presence of

hydroxide ( $\text{OH}^-$ ) and absorbed water at surface.<sup>[58]</sup> The assigned binding energies are W (31.8 eV),  $\text{W}^{4+}$  (32.7 eV),  $\text{W}^{5+}$  (33.8 eV), and  $\text{W}^{6+}$  (36.2 eV) for W 4f<sub>7/2</sub>;  $\text{O}^{2-}$  (530.8 eV),  $\text{OH}^-$  (531.9 eV) and  $\text{H}_2\text{O}$  (533.2 eV) for O 1s.<sup>[58–60]</sup> TEM diffraction patterns and lattice fringes also suggest the presence of  $\text{WO}_3$  as a dissolution product (Figure 4i). Such surface structure is similar to that of bulk W materials exposed to acidic solution, as reported by Lillard et al., where an inner  $\text{WO}_3$  layer and an outer loosely bound W hydroxide layer occur.<sup>[61]</sup>

As shown in Figure 5j,k, the evolution of surface chemistry for Mo is similar to that for W, with an initial  $\text{MoO}_3$  native oxide, then a mixture of valence oxides ( $\text{Mo}^{4+}$ ,  $\text{Mo}^{5+}$ , and  $\text{Mo}^{6+}$ ) as dissolution products, with terminal formation of  $\text{Mo}^{5+}$  oxide after 80 d. The presence of hydroxide and sometimes absorbed water are also observed on the Mo surface based on the XPS O 1s data (Figure 5k). The assigned binding energies are Mo (228.7 eV),  $\text{Mo}^{4+}$  (229.5 eV),  $\text{Mo}^{5+}$  (230.9 eV), and  $\text{Mo}^{6+}$  (233.0 eV) for Mo 3d<sub>5/2</sub>;  $\text{O}^{2-}$  (530.7 eV),  $\text{OH}^-$  (531.8 eV), and  $\text{H}_2\text{O}$  (533.0 eV) for O 1s.<sup>[36,62]</sup> The TEM results of Mo in Figure 5i support the presence of  $\text{MoO}_3$  and  $\text{MoO}_2$ . These findings are consistent with reported dissolution surface chemistry of bulk Mo materials in aqueous solution.<sup>[36,63]</sup> Degradation of W and Mo in salt solutions with different pH values follows dissolution patterns similar to those in DI water. The pH can affect

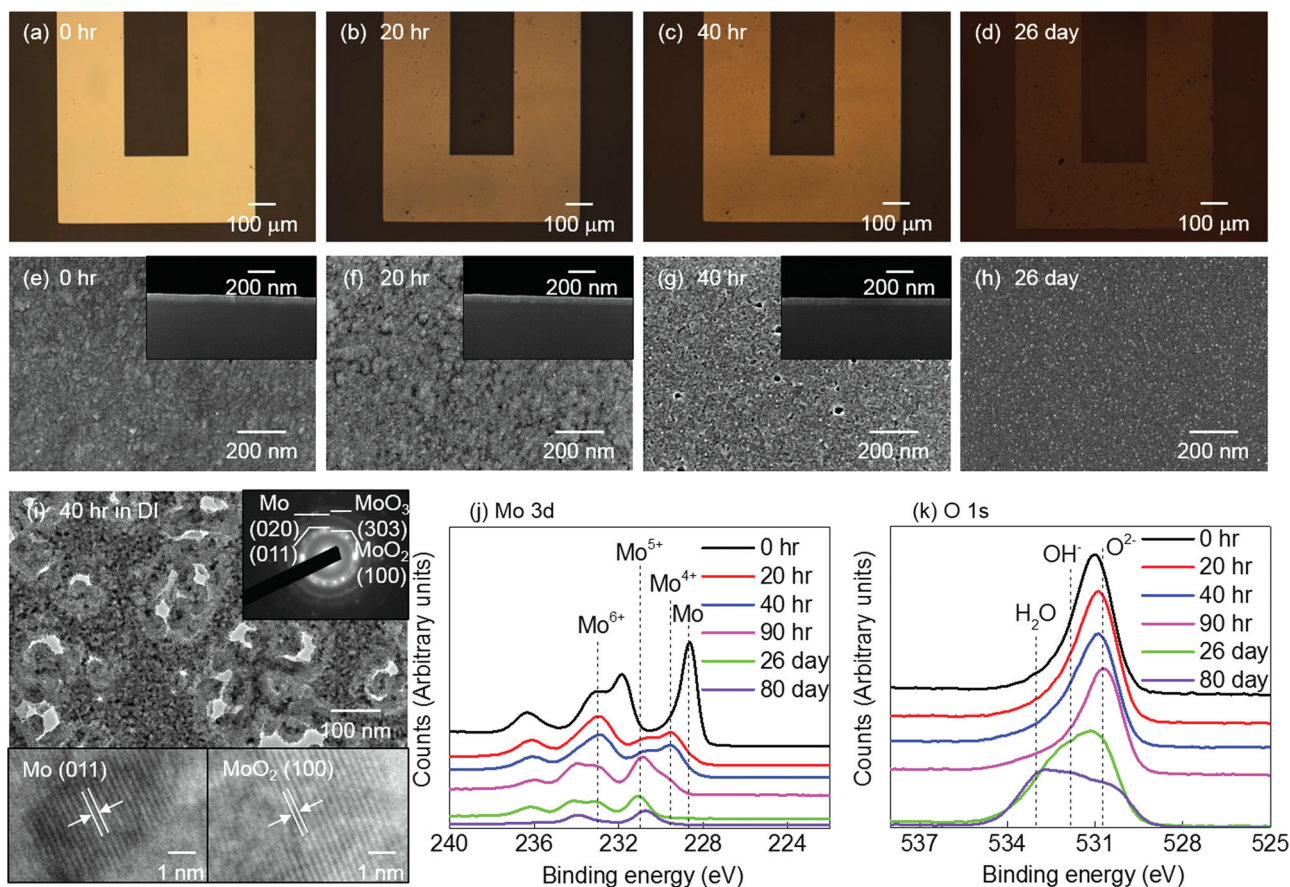


**Figure 5.** Evolution of microstructure and surface chemistry associated with dissolution of Mo in DI water. a–d) optical images; e–h) SEM images with cross-sectional views in the insets; i) TEM bright field image with diffraction patterns and lattice fringes; j–k) XPS data.

the relative concentrations of the various mixed valence surface oxides in ways that can alter the dissolution rate.<sup>[28,63,64]</sup>

Due to the solubility of  $\text{WO}_x$  and  $\text{MoO}_x$ ,<sup>[27,65]</sup> both W and Mo can slowly degrade in water. The EDR is  $\approx 2\text{--}3$  times faster than the rate of change in thickness (Table 1), due to the formation of micropores (Figures 4,5c,g,i). The corrosion products  $\text{WO}_x$  and  $\text{MoO}_x$  require time to fully dissolve after the disappearance of the metals; increasing the basicity can accelerate the rates.<sup>[27,65,66]</sup> As shown in Figures 4,5j, the slowly decreasing peak to background XPS signals of W and Mo suggest the gradual dissolution of  $\text{WO}_x$  and  $\text{MoO}_x$  in DI water, with an estimated residual thickness of 10–20 nm after  $\approx 70$  d, as indicated by the continued presence of XPS signal up to this point. These oxides are expected to completely disappear given sufficient time. The dissolution rates of W and Mo oxides are estimated to be  $\approx 0.2\text{--}0.5$  nm  $\text{d}^{-1}$ . It is noted that the substrate signal appears after 31 d and 26 d for W and Mo respectively, and therefore distorts the O 1s peaks to a certain level.

### 2.2.3. Zn and Fe

Non-uniform dissolution dominates in the cases of Zn and Fe thin films in DI water, as shown in Figures 6,7a–d. Pitting nucleates in random locations and then spreads across the

films. Such corrosion is commonly observed in bulk samples of Zn and Fe in aqueous solutions.<sup>[35,67,68]</sup>

The evolution of surface morphology for Zn is illustrated in Figure 6e–h, where both petal-like and fiber-like dissolution products are observed. Independent of the morphology, the surface products are identified to be mainly ZnO and  $\text{Zn}(\text{OH})_2$  with occasional presence of a certain amount of carbonates, as the XPS data shows in Figure 6j,k. The assigned binding energies of O 1s are Zn-O (530.4 eV), Zn-(OH) (531.8 eV), and carbonates (530.0 eV).<sup>[69]</sup> The Zn  $2p_{3/2}$  peak (remaining at 1021.8 eV) does not shift in accordance with O 1s as shown in Figure 6j, and therefore cannot be unambiguously separated. The labeled binding energies of Zn  $2p_{3/2}$  in Figure 6j are Zn (1021.6 eV), Zn-O (1021.7 eV), and Zn-OH (1022.4 eV).<sup>[69,70]</sup> The TEM diffraction patterns and lattice fringes confirm the presence of ZnO on the surface (Figure 6i). The TEM bright field image also illustrates a porous morphology and a non-uniform distribution of surface oxide, with more ZnO present on the left part of the image (Figure 6i). Dissolution of Zn thin films in Hanks' solutions shows similar non-uniform behavior, where the products are also expected to be mainly ZnO and  $\text{Zn}(\text{OH})_2$  as for bulk Zn materials.<sup>[35]</sup> Such Zn oxide layers are only partially protective and have relatively high solubility in aqueous solution.<sup>[35]</sup>

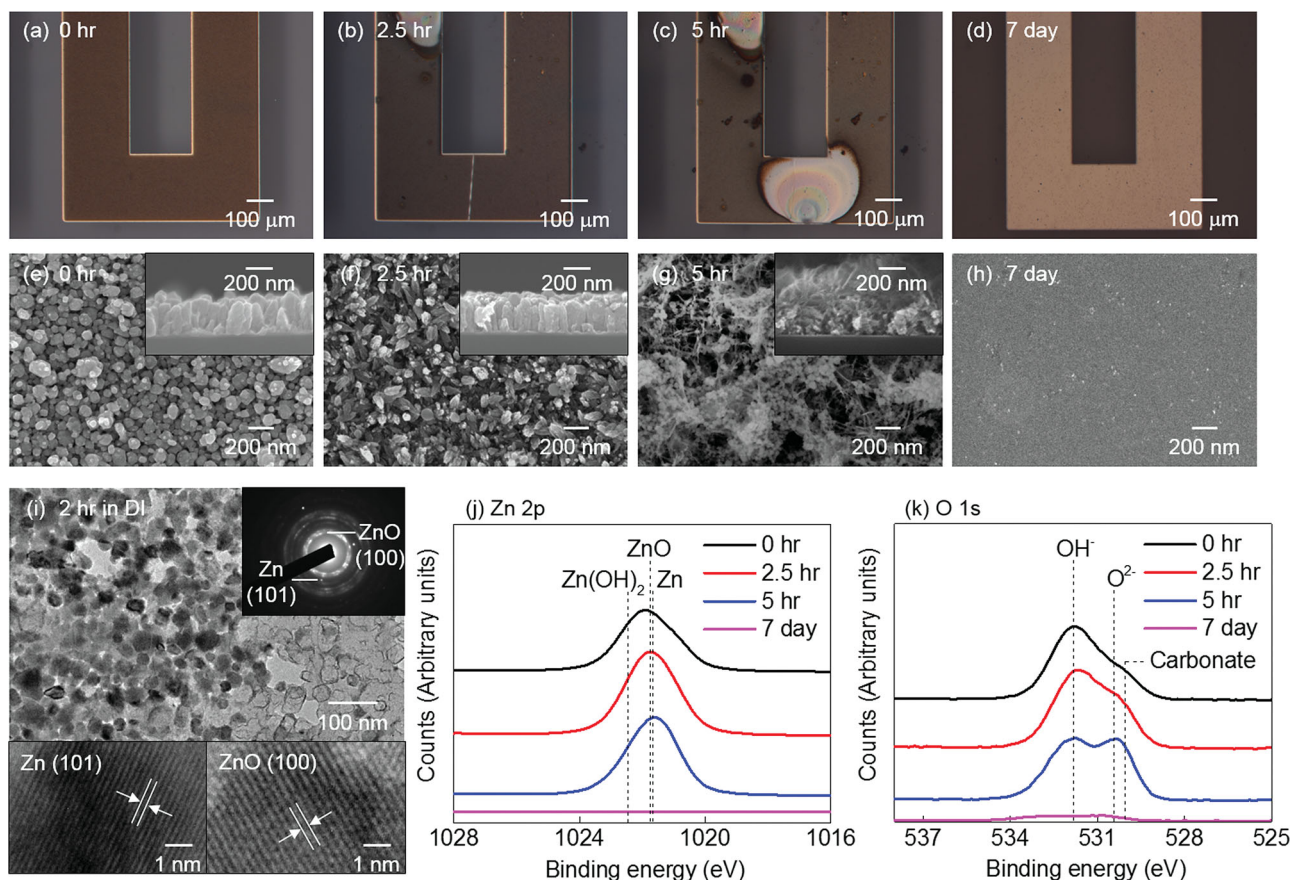


**Figure 6.** Evolution of microstructure and surface chemistry associated with dissolution of Zn in DI water. a–d) optical images; e–h) SEM images with cross-sectional views in the insets; i) TEM bright field image with diffraction patterns and lattice fringes; j,k) XPS data.

The surface morphologies of dissolution products for the case of Fe appear in Figure 7f–h. The XPS data (Figure 7j,k) suggest that the surface layer is  $\text{Fe}_2\text{O}_3$  and hydroxide, with Fe  $2p_{3/2}$  for Fe (706.9 eV) and O 1s for  $\text{Fe}_2\text{O}_3$  (529.8 eV) and hydroxide (531.2 eV).<sup>[71,72]</sup> The TEM diffraction patterns and lattice fringes (Figure 7i) indicate the presence of  $\text{Fe}_3\text{O}_4$ , which is a common corrosion product that forms after the hydroxide in the presence of excessive oxygen.<sup>[20]</sup> The presence of Fe oxides can help passivate the propagation of pits and simultaneously reduce the dissolution rate. The long incubation for pitting initiation in different locations and the passivation effects might cause the observed plateaus in time dependence of the resistance (Figure 1g). Although Zn also shows non-uniform patterns of dissolution, the facile initiation of pits and high reaction rates eliminate plateaus in dissolution (Figure 1d). The degradation behavior of Fe in Hanks' solution is similar to that in DI water except at pH 5, for which uniform dissolution and absence of obvious surface oxides are observed, resulting from the acidic environment.<sup>[21]</sup>

Similar to other transient metals, Zn thin films cease to be electrical continuous far sooner ( $\approx 10$  times faster) than the thickness decreases to zero (Table 1, Figures 1d, 6c). The hydrolysis products dissolve completely after about 5–7 d (Figure 6d,h,i). The dissolution rates of Zn oxides are estimated to be roughly  $\approx 120\text{--}170\text{ nm day}^{-1}$ . By contrast, the Fe oxides do

not dissolve even after one month. Furthermore, the final total thickness is more than 10 times larger than the initial value (Figure 1i). Such retention of Fe oxides was also observed by in vivo tests.<sup>[9]</sup> These types of behaviors are generally undesirable for transient electronic systems.

Multiple options in transient metals that are fully dissolvable (both metals and dissolution oxide products) enable selection of materials to match requirements for degradation times in different applications. For example, medical devices that require direct contact of metals with biological tissues for signal sensing benefit from metals that have slow but predictable degradation rates (e.g., W and Mo); other applications such as secure electronics might benefit from rapid transience (e.g., Mg and Zn). For materials such as Fe, the long term retention of oxide products may make it unsuitable for many types of transient electronic systems. Moreover, various microstructures develop for the different metals during their dissolution. Generally, a predictable and uniform loss of mass that tracks closely the loss in conductivity is preferred. As in the case of rate, the requirements associated with a particular application will define the importance of morphology. Transport issues upon dissolution can also be important. The reaction products will accumulate near the thin film surface and, as a result, could potentially slow the reaction as dissolution proceeds, depending on whether surface reaction or diffusion of products into the

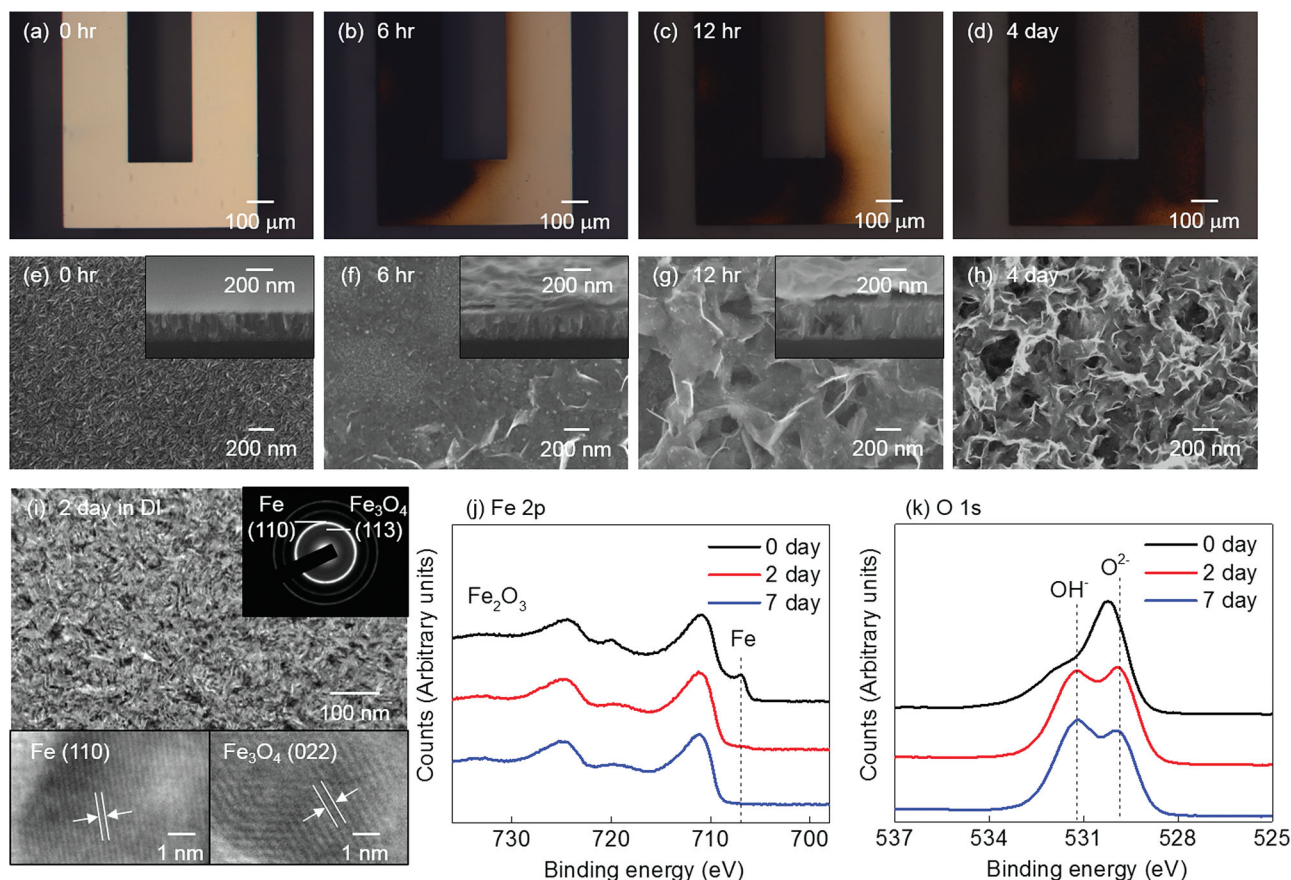


**Figure 7.** Evolution of microstructure and surface chemistry associated with dissolution of Fe in DI water. a–d) optical images; e–h) SEM images with cross-sectional views in the insets; i) TEM bright field image with diffraction patterns and lattice fringes; j, k) XPS data.

bulk solution is rate limiting. Dissolution could be therefore faster in flowing fluids. However, this effect is expected to be less important in metals with slow surface reaction kinetics (e.g., Fe, W, and Mo) and in metal thin films with small areas.

### 2.3. Degradation of Thin Film Transistors with Transient Metal Contacts

Mg (300 nm), AZ31B Mg alloy (300 nm), Zn (300 nm), W (150 nm), and Mo (80 nm), each without the Cr adhesion layer, are used as contacts for n-channel MOSFETs to demonstrate the feasibility of building transient systems based on these metals. The geometry of the devices, which are constructed on silicon-on-insulation (SOI) wafers, is illustrated in **Figure 8a**. The n-type region is doped with phosphorous at concentration  $\approx 10^{20} \text{ cm}^{-3}$ , with  $\text{SiO}_2$  formed by plasma-enhanced chemical vapor deposition (PECVD) as the gate dielectric. The lengths ( $L$ ) and widths ( $W$ ) of the channels in all cases are 50  $\mu\text{m}$  and 400  $\mu\text{m}$ , respectively. The typical on/off ratios and mobilities are  $>10^4$  and  $250 \text{ cm}^2 \text{ V}^{-1} \text{ s}^{-1}$  respectively, regardless of the type of metal. The data suggest negligible effects of contact resistance, due partly to the relatively large  $L$ . Detailed studies of contacts lie beyond the scope of the present work.

Images and data related to the functional degradation of these MOSFETs induced by immersion in DI water appear in **Figure 8b–f** and **Figure 9**. Due to the relatively fast dissolution rate for the metals ( $\approx 1 \times 10^{-3}$ – $0.3 \mu\text{m h}^{-1}$ ) compared to the silicon and PECVD silicon oxide ( $\approx 0.01$ – $1 \text{ nm d}^{-1}$ ),<sup>[1,73]</sup> the degradation in functionality mainly results from the loss of the contacts as the dissolution proceeds. As can be seen in **Figure 8**, MOSFETs with Mg, AZ31B alloy and Zn contacts cease to function after  $\approx 2$ – $8 \text{ h}$  (corresponding to EDRs of  $\approx 0.04$ – $0.15 \mu\text{m h}^{-1}$  estimated by dividing the metal thickness over the time required to lose function), while those with W and Mo exhibit stable operation for  $\approx 12 \text{ h}$  and  $\approx 25 \text{ h}$ , respectively. These results are consistent with expectation based on the dissolution rates.

After the disappearance of metals and their residual oxides, the phosphorous doped silicon and PECVD silicon oxide can slowly dissolve away. It is known that silicon and silicon oxide can dissolve to  $\text{Si(OH)}_4$  in basic solutions, with rates that depend on temperature and the concentration of  $\text{H}_2\text{O}$  and  $\text{OH}^-$ <sup>[74]</sup> and, for silicon, on the doping type and level.<sup>[75]</sup> Studies of dissolution of  $\text{SiO}_2$  (amorphous silica or quartz) in water at RT, and depending on the structure and quality, reveals rates that range from  $\approx 10^{-4}$ – $10^{-1} \text{ nm d}^{-1}$ .<sup>[76,77]</sup> Although only limited data exist for PECVD  $\text{SiO}_2$ , the rates can be expected to vary over a large range depending on the structure and density of

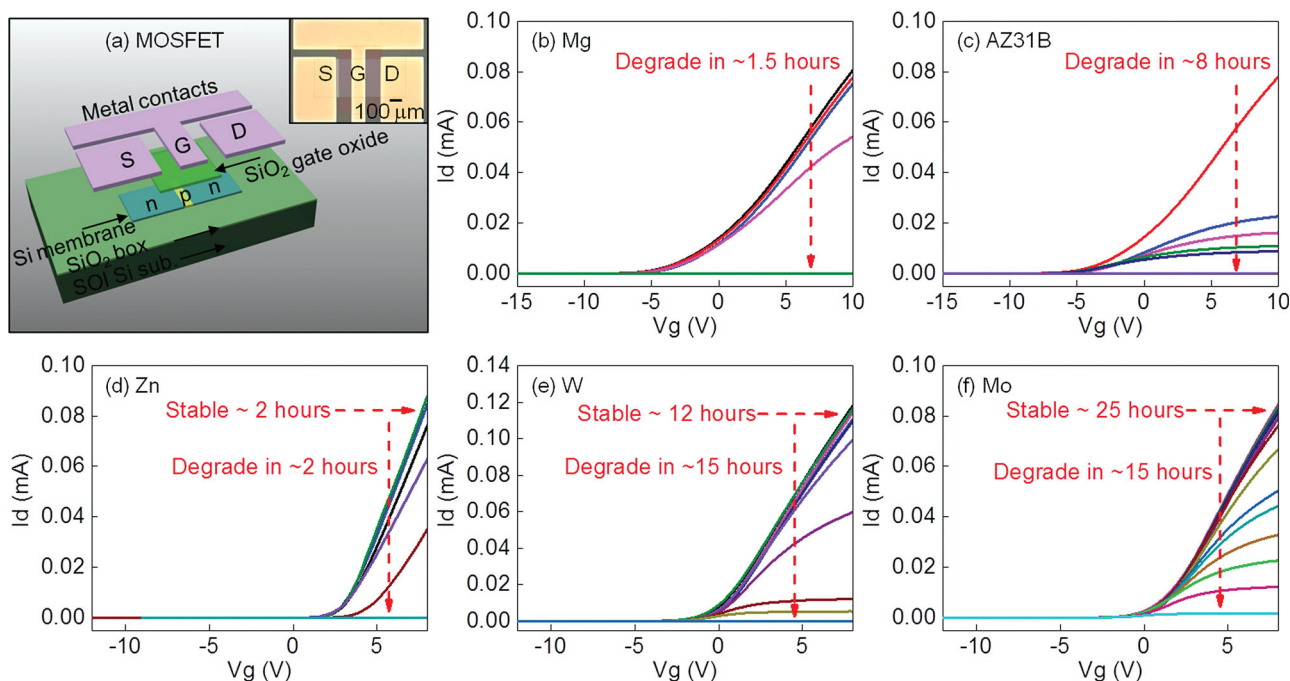


**Figure 8.** a) Geometry of an n-channel MOSFET, with a top view optical micrograph in the inset; b–f) functional degradation of n-channel MOSFETs, as evaluated through measurements of the drain current ( $I_d$ ) as a function of gate voltage ( $V_g$ ) for a drain bias ( $V_d$ ) of 0.2 V, with transient metal contacts: Mg, AZ31B Mg alloy, Zn, W, and Mo respectively.

the films. Reported results for amorphous silica can, nevertheless, be used as a reference, with rates approximately ten times faster than those for quartz.<sup>[76]</sup> Silicon nanoparticles and porous silicon are reported to reactively dissolve at physiological conditions,<sup>[78,79]</sup> with rates in lightly doped films of Si of  $\approx 2 \text{ nm day}^{-1}$  in pH 7.4 phosphate buffered saline (PBS) at RT.<sup>[1]</sup> For phosphorous doping at  $\approx 5 \times 10^{20} \text{ cm}^{-3}$ , the rates, as observed in basic solutions, can decrease by a factor of 4.<sup>[75]</sup> To confirm the dissolution of the phosphorous doped ( $\approx 10^{20} \text{ cm}^{-3}$ ) n-type Si and the PECVD  $\text{SiO}_2$  gate oxides in Hanks' solution pH 7.4 at RT, the thicknesses of each were measured as a function of time. **Figure 10** shows the results  $\approx 0.6$  and  $0.25 \text{ nm day}^{-1}$  for n-doped Si and  $\text{SiO}_2$  respectively. The dissolution rates fall in reasonable range compared to the reported results.

### 3. Conclusions

The results presented here describe in detail the electrical consequences of reactive dissolution of thin film patterned traces of Mg, AZ31B Mg alloy, Zn, Fe, W, and Mo in de-ionized (DI) water and simulated body fluids (Hanks' solution pH 5–8). These findings, combined with measured changes in morphology and chemistry, provide connection to previous corrosion studies of these materials in bulk form. Use of the metals as contacts and electrodes in n-channel Si MOSFETs demonstrate one area of possible applications in transient electronics. The following conclusions are important in this context: 1) the EDRs of Mg, AZ31B Mg alloy, and Zn ( $\approx 0.5\text{--}3 \mu\text{m h}^{-1}$ ) are much higher than those of W, Mo, and Fe ( $\approx 10^{-4}\text{--}0.02 \mu\text{m h}^{-1}$ ).

The effects of pH and temperature are consistent with studies of bulk corrosion. 2) Oxides as dissolution products appear on exposed surfaces, with chemistry and structure similar to that observed in bulk materials. 3) The dissolution of thin films involves two stages, beginning with a fast degradation of the base metal followed by dissolution of residual oxides. Such oxides on Mg, AZ31B Mg alloy, and Zn of 300 nm fully disappear within one week in DI water. For W (150 nm) and Mo (40 nm), these residual oxides have thicknesses of  $\approx 20\text{--}40 \text{ nm}$  and are expected to completely dissolve after several months. By contrast, iron oxides are relatively insoluble. 4) Mg, AZ31B Mg alloy, Zn, W, and Mo can be used as transient contacts for silicon MOSFETs. Degradation in function upon immersion into aqueous solutions results from the dissolution of metal; the Si and  $\text{SiO}_2$  disappear on comparatively long timescales.

### 4. Experimental Section

Patterned, serpentine traces of thin metal films (40–300 nm) deposited by electron beam evaporation (Fe) (AJA Orion 3 sputter system, N. Scituate, MA) or by magnetron sputtering (all others) (AJA Orion 8 evaporation system, N. Scituate, MA) were patterned by photolithography (AZ nLOF 2070 photoresist) and lift-off on glass substrates. The deposition conditions were  $0.1 \text{ nm s}^{-1}$  for Fe; 50 W, 3 mT for Mg and AZ31B Mg alloy; 100 W, 100 mT for Zn; 150 W 5 mT for W; 150 W 3 mT for Mo. These conditions minimize delamination and maintain high quality, uniform films with good yield. A layer of Cr (10 nm) deposited by either sputtering or electron beam evaporation served as an adhesion promoter, to eliminate delamination during the dissolution tests. The CVD W (150 nm) samples were provided by MIT Lincoln Laboratory. Grain size of the deposited thin films was

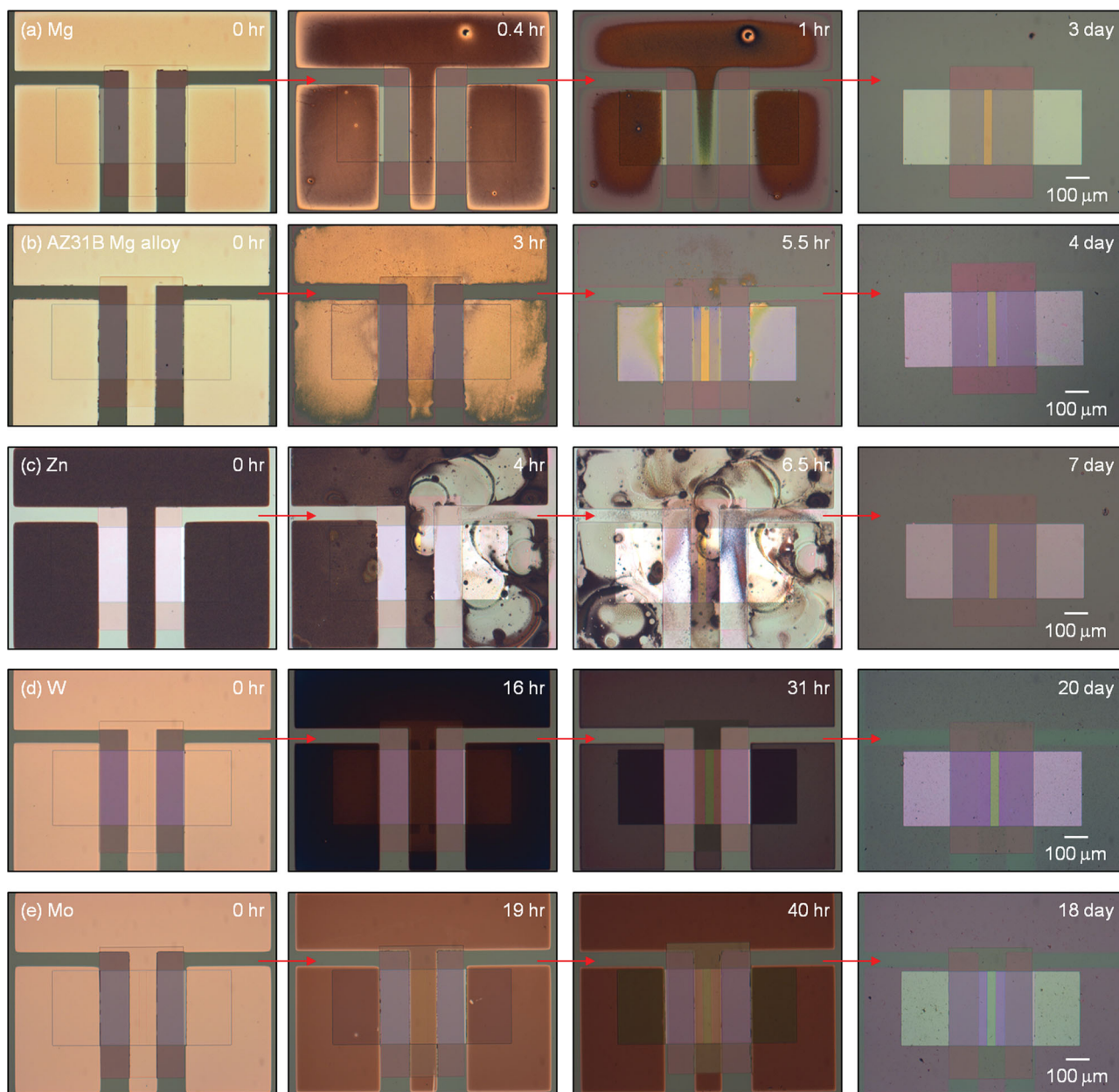


**Figure 9.** Dissolution of metal contacts in transient n-channel MOSFETs: a) Mg, b) AZ31B Mg alloy, c) Zn, d) W, and e) Mo.

evaluated from X-ray diffraction (XRD) data analyzed with Jade software: Fe (10 nm); Mg (22 nm); AZ31B (24 nm); Zn (13 nm); sputtered W (16 nm); CVD W (55 nm); and Mo (30 nm).

Dissolution behavior was studied in naturally aerated DI water and Hanks' solution (H 8264, Sigma-Aldrich, St. Louis, MO). As a control experiment with Mo (40 nm thick, in Hanks' solution at pH 8, for 250 h), air was continuously bubbled through the solution. The dissolution rate was found to be similar to those without bubbling. Given the known sensitivity of Mo dissolution to  $O_2$  concentration, this result suggests that the  $O_2$  concentration in the solutions is in equilibrium with air and does not vary significantly over time. Small amounts of NaOH and HCl were added to the Hanks' solutions to control the pH. A Hanna HI 9126 portable pH/ORP meter (HANNA instruments, Smithfield, RI) was used to monitor the pH at various times during dissolution, to ensure that the value remained constant during the experiment ( $\pm 0.2$  pH units). Furnace with constant temperature of 37 °C was used to conduct dissolution at

body temperature. Electrical probing occurred through contacts to two pads located outside of the solution. The thicknesses of patterned metal thin films in DI water were also monitored, even after complete loss of electrical continuity, with solutions replaced every other day to avoid reaching the solubility limits.

N-channel MOSFETs were prepared on silicon-on-insulator (SOI) wafers (320 nm top silicon layer, p-type, SOITEC, France). The source and drain areas were doped through diffusion of phosphorous at  $\approx 1000$  °C for five minutes with thermal oxides as the doping mask, to yield a concentration of  $\approx 10^{20}$  cm $^{-3}$ . The top device silicon was patterned by reactive ion etching (RIE) with sulfur hexafluoride ( $SF_6$ ) gas. The gate dielectrics ( $SiO_2$ ,  $\approx 130$  nm) were formed by plasma-enhanced chemical vapor deposition (PECVD) at 250 °C, and patterned by photolithography and etching in buffered oxide etchant (BOE). Metal contacts were deposited using the same methods as mentioned previously, but without the Cr adhesion layer. The transient electrical properties of the MOSFETs

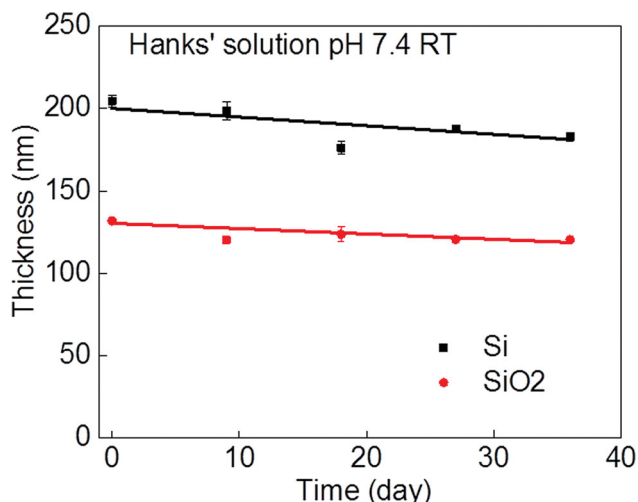


**Figure 10.** Change in thickness of n-type Si (phosphorous concentration  $\approx 10^{20} \text{ cm}^{-3}$ ) and PECVD SiO<sub>2</sub> in an n-channel MOSFET upon dissolution in Hanks' solution pH 7.4 at RT.

were evaluated using a probe station and semiconductor parameter analyzer (Agilent 4155C, Agilent Technologies, Santa Clara, CA).

A Hitachi S-4800 high resolution SEM (Hitachi high-technologies corporation, Japan) was used to examine the surface and cross-sectional morphologies of metal films at various stages of dissolution in DI water, using 10 kV applied voltage and 4 mm working distance. The surface chemistry was determined by using XPS. High-resolution XPS measurements were made with a Kratos Axis Ultra photoelectron spectrometer (Kratos Analytical, Inc., Manchester, UK) using monochromatic Al K $\alpha$  radiation (1486.6 eV) at a pass energy of 40 eV. The binding energy scale was referenced to the adventitious C 1s signal at 285 eV (except for Mg and Mg alloys which were referenced to 286 eV). The dissolution products and film morphologies were also studied by JEOL 2010LaB<sub>6</sub> transmission electron microscope (TEM, JEOL USA, Inc., Peabody, MA), with an applied voltage of 200 kV and camera constant of 13.4 mm. TEM samples were prepared by depositing 100 nm of Mg and AZ31B Mg alloy, and 50 nm of Zn, W, Mo, and Fe on 15 nm silicon nitride grids (Ted Pella, Inc., Redding, CA). These samples were immersed in DI water for 0.5 h (Mg), 1 h (AZ31B Mg alloy), 10 h (W), 40 h (Mo), 2 h (Zn), and 2 d (Fe) before TEM analysis. A surface profilometer (Veeco/Sloan Dektak 3 ST, Plainview, New York) was used to determine the changes in thicknesses of metal thin films at various stages of dissolution in DI water. Thickness changes of phosphor doped Si and PECVD SiO<sub>2</sub> gate oxides in MOSFETs upon dissolution in Hanks' solution pH 7.4 at RT were measured by atomic force microscope (AFM, Cypher, Asylum Research, Santa Barbara, CA). The solution was replaced every other day to avoid solubility limits. The reported thickness data correspond to averages of thicknesses evaluated at ten different locations. The standard deviations of these data were used as the error bars.

## Supporting Information

Supporting Information is available from the Wiley Online Library or from the author.

## Acknowledgements

Financial support from Defense Advanced Research Projects Agency (DARPA) and the National Science Foundation (NSF, DMR-12-42240) enabled the experimental and theoretical work, respectively. We thank

MIT Lincoln Laboratory for providing the CVD W samples. This work was carried out in part in the Frederick Seitz Materials Research Laboratory Central Facilities, University of Illinois. These acknowledgements were updated on February 5, 2014.

Received: May 29, 2013

Revised: July 15, 2013

Published online: September 25, 2013

- [1] S.-W. Hwang, H. Tao, D.-H. Kim, H. Cheng, J.-K. Song, E. Rill, M. A. Brenckle, B. Panilaitis, S. M. Won, Y.-S. Kim, Y. M. Song, K. J. Yu, A. Ameen, R. Li, Y. Su, M. Yang, D. L. Kaplan, M. R. Zakin, M. J. Slepian, Y. Huang, F. G. Omenetto, J. A. Rogers, *Science* **2012**, 337, 1640.
- [2] C. Dagdeviren, S.-W. Hwang, Y. Su, S. Kim, H. Cheng, O. Gur, R. Haney, F. G. Omenetto, Y. Huang, J. A. Rogers, *Small* **2013**, 10.1002/sml.201300146.
- [3] S.-W. Hwang, D.-H. Kim, H. Tao, T.-i. Kim, S. Kim, K. J. Yu, B. Panilaitis, J.-W. Jeong, J.-K. Song, F. G. Omenetto, J. A. Rogers, *Adv. Funct. Mater.* **2013**, 10.1002/adfm.201300127.
- [4] S.-W. Hwang, X. Huang, J.-H. Seo, J.-K. Song, S. Kim, S. Hage-Ali, H.-J. Chung, H. Tao, F. G. Omenetto, Z. Ma, J. A. Rogers, *Adv. Mater.* **2013**, 25, 3526.
- [5] C. J. Bettinger, Z. Bao, *Adv. Mater.* **2010**, 22, 651.
- [6] L. E. Bevers, P.-L. Hagedoorn, W. R. Hagen, *Coord. Chem. Rev.* **2009**, 253, 269.
- [7] D. G. Barceloux, *J. Toxicol.: Clin. Toxicol.* **1999**, 37, 231.
- [8] P. Trumbo, A. A. Yates, S. Schlicker, M. Poos, *J. Am. Dietetic Assoc.* **2001**, 101, 294.
- [9] P. P. Mueller, S. Arnold, M. Badar, D. Bormann, F.-W. Bach, A. Drynda, A. Meyer-Lindenberg, H. Hauser, M. Peuster, *J. Biomed. Mater. Res., Part A* **2012**, 100A, 2881.
- [10] H. Hermawan, A. Purnama, D. Dube, J. Couet, D. Mantovani, *Acta Biomater.* **2010**, 6, 1852.
- [11] R. Zeng, W. Dietzel, F. Witte, N. Hort, C. Blawert, *Adv. Eng. Mater.* **2008**, 10, B3.
- [12] F. Witte, *Acta Biomater.* **2010**, 6, 1680.
- [13] N. T. Kirkland, N. Biribilis, M. P. Staiger, *Acta Biomater.* **2012**, 8, 925.
- [14] H. Wang, Z. Shi, *J. Biomed. Mater. Res., Part B* **2011**, 98B, 203.
- [15] J. Walker, S. Shadanbaz, N. T. Kirkland, E. Stace, T. Woodfield, M. P. Staiger, G. J. Dias, *J. Biomed. Mater. Res., Part B* **2012**, 100B, 1134.
- [16] W. F. Ng, K. Y. Chiu, F. T. Cheng, *Mater. Sci. Eng. C* **2010**, 30, 898.
- [17] G. L. Song, *Corrosion Sci.* **2007**, 49, 1696.
- [18] F. L. Nie, Y. F. Zheng, S. C. Wei, C. Hu, G. Yang, *Biomed. Mater.* **2010**, 5, 1.
- [19] S. F. Zhu, N. Huang, L. Xu, Y. Zhang, H. Q. Liu, H. Sun, Y. X. Leng, *Mater. Sci. Eng. C* **2009**, 29, 1589.
- [20] E.-S. M. Sherif, R. M. Erasmus, J. D. Comins, *Electrochim. Acta* **2010**, 55, 3657.
- [21] R. W. Revie, H. H. Uhlig, *Corrosion and corrosion control: An introduction to corrosion science and engineering*, 4th ed., John Wiley & Sons, Inc, Hoboken, NJ **2008**.
- [22] M. Peuster, C. Hesse, T. Schloo, C. Fink, P. Beerbaum, C. von Schnakenburg, *Biomaterials* **2006**, 27, 4955.
- [23] U. Schwertmann, *Plant Soil* **1991**, 130, 1.
- [24] P. K. Bowen, J. Drelich, J. Goldman, *Adv. Mater.* **2013**, 10.1002/adma.201300226.
- [25] J. Zhou, N. S. Xu, Z. L. Wang, *Adv. Mater.* **2006**, 18, 2432.
- [26] E. Patrick, M. E. Orazem, J. C. Sanchez, T. Nishida, *J. Neurosci. Meth.* **2011**, 198, 158.
- [27] W. A. Badawy, F. M. Al-Kharafi, *Electrochim. Acta* **1998**, 44, 693.

- [28] M. Anik, K. Osseo-Asare, *J. Electrochem. Soc.* **2002**, 149, B224.
- [29] M. Peuster, C. Fink, C. von Schnakenburg, *Biomaterials* **2003**, 24, 4057.
- [30] N. Strigul, *Ecotoxicol. Environ. Safety* **2010**, 73, 1099.
- [31] L. De Rosa, C. R. Tomachuk, J. Springer, D. B. Mitton, S. Saiello, F. Bellucci, *Mater. Corrosion* **2004**, 55, 602.
- [32] *Uhlig's corrosion handbook*. 3rd ed., (Ed. R. W. Revie), John Wiley & Sons, Inc, Hoboken, NJ **2011**.
- [33] G. Song, A. Atrens, *Adv. Eng. Mater.* **2003**, 5, 837.
- [34] R. Ambat, N. N. Aung, W. Zhou, *J. Appl. Electrochem.* **2000**, 30, 865.
- [35] X. G. Zhang, *Corrosion and electrochemistry of zinc*, Plenum Press, New York **1996**.
- [36] H. Hixson, P. M. A. Sherwood, *J. Chem Soc.* **1995**, 91, 3593.
- [37] H. Oikawa, *Jpn. J. Appl. Phys.* **1975**, 14, 629.
- [38] W. Lang, R. Zander, *Ind. Eng. Chem. Fundam.* **1986**, 25, 775.
- [39] K. M. S. Youssef, C. C. Koch, P. S. Fedkiw, *Corrosion Sci.* **2004**, 46, 51.
- [40] E. A. Kneer, C. Raghunath, V. Mathew, S. Raghavan, J. S. Jeon, *J. Electrochem. Soc.* **1997**, 144, 3041.
- [41] C. Blawert, V. Heitmann, N. Scharnagl, M. Stormer, J. Lutz, A. Prager-Duschke, D. Manova, S. Mandl, *Plasma Proc. Polym.* **2009**, 6, S690.
- [42] K. Miyake, K. Ohashi, H. Takahashi, T. Minemura, *Surf. Coatings Technol.* **1994**, 65, 208.
- [43] K. Schluter, C. Zamponi, A. Piorra, E. Quandt, *Corrosion Sci.* **2010**, 52, 3973.
- [44] R. Li, H. Cheng, Y. Su, S.-W. Hwang, L. Yin, H. Tao, M. A. Brenckle, D.-H. Kim, F. G. Omenetto, J. A. Rogers, Y. Huang, *Adv. Funct. Mater.* **2013**, 23, 3106.
- [45] J. Thurn, *J. Non-Crystalline Solids* **2008**, 354, 5459.
- [46] K. M. Davis, M. Tomozawa, *J. Non-Crystalline Solids* **1995**, 185, 203.
- [47] M.-C. Zhao, P. Schmutz, S. Brunner, M. Liu, G.-I. Song, A. Atrens, *Corrosion Sci.* **2009**, 51, 1277.
- [48] A. Samaniego, I. Llorente, S. Feliu Jr., *Corrosion Sci.* **2013**, 68, 66.
- [49] Y. Jang, B. Collins, J. Sankar, Y. Yun, *Acta Biomater.* **2013**, <http://dx.doi.org/10.1016/j.bbr.2011.03.031>.
- [50] G. Wu, W. Dai, L. Song, A. Wang, *Mater. Lett.* **2010**, 64, 475.
- [51] M. Liu, S. Zanna, H. Ardelean, I. Frateur, P. Schmutz, G. Song, A. Atrens, P. Marcus, *Corrosion Sci.* **2009**, 51, 1115.
- [52] M. Santamaria, F. Di Quarto, S. Zanna, P. Marcus, *Electrochim. Acta* **2007**, 53, 1314.
- [53] D. Tie, F. Feyerabend, N. Hort, R. Willumeit, D. Hoeche, *Adv. Eng. Mater.* **2010**, 12, B699.
- [54] H. B. Yao, Y. Li, A. T. S. Wee, *Appl. Surf. Sci.* **2000**, 158, 112.
- [55] N. I. Zainal Abidin, D. Martin, A. Atrens, *Corrosion Sci.* **2011**, 53, 862.
- [56] M. Taheri, R. C. Phillips, J. R. Kish, G. A. Botton, *Corrosion Sci.* **2012**, 59, 222.
- [57] *CRC handbook of chemistry and physics*, 93th ed., (Ed. W. M. Haynes and D. R. Lide), CRC Press, Boca Raton, FL **2012**.
- [58] A. P. Shpak, A. M. Korduban, M. M. Medvedskij, V. O. Kandyba, *J. Electron Spectrosc. Rel. Phenom.* **2007**, 156, 172.
- [59] F. Y. Xie, L. Gong, X. Liu, Y. T. Tao, W. H. Zhang, S. H. Chen, H. Meng, J. Chen, *J. Electron Spectrosc. Rel. Phenom.* **2012**, 185, 112.
- [60] D. Barreca, G. Carta, A. Gasparotto, G. Rossetto, E. Tondello, P. Zanella, *Surf. Sci. Spectra* **2001**, 8, 258.
- [61] R. S. Lillard, G. S. Kanner, D. P. Butt, *J. Electrochem. Soc.* **1998**, 145, 2718.
- [62] I. A. Okonkwo, J. Doff, A. Baron-Wiecheć, G. Jones, E. V. Koroleva, P. Skeldon, G. E. Thompson, *Thin Solid Films* **2012**, 520, 6318.
- [63] M. Petrova, M. Bojinov, S. Zanna, P. Marcus, *Electrochim. Acta* **2011**, 56, 7899.
- [64] D. Tamboli, S. Seal, V. Desai, A. Maury, *J. Vac. Sci. Technol. A* **1999**, 17, 1168.
- [65] M. Anik, T. Cansizoglu, *J. Appl. Electrochem.* **2006**, 36, 603.
- [66] A. B. Stefaniak, *Part. Fibre Toxicol.* **2010**, 7, 38.
- [67] H. Wang, J. Xie, K. P. Yan, M. Duan, Y. Zuo, *Corrosion Sci.* **2009**, 51, 181.
- [68] Z. H. Dong, W. Shi, X. P. Guo, *Corrosion Sci.* **2011**, 53, 1322.
- [69] N. J. Nicholas, G. V. Franks, W. A. Ducker, *CrystEngComm* **2012**, 14, 1232.
- [70] B. C. Lin, P. Shen, S. Y. Chen, *J. Phys. Chem. C* **2010**, 115, 5003.
- [71] D. Barreca, G. A. Battiston, D. Berto, R. Gerbasi, E. Tondello, *Surf. Sci. Spectra* **2001**, 8, 240.
- [72] S. Suzuki, K. Yanagihara, K. Hirokawa, *Surf. Interface Anal.* **2000**, 30, 372.
- [73] Unpublished results.
- [74] H. Seidel, L. Csepregi, A. Heuberger, H. Baumgartel, *J. Electrochem. Soc.* **1990**, 137, 3612.
- [75] H. Seidel, L. Csepregi, A. Heuberger, H. Baumgartel, *J. Electrochem. Soc.* **1990**, 137, 3626.
- [76] J. P. Icenhower, P. M. Dove, *Geochim. Cosmochim. Acta* **2000**, 64, 4193.
- [77] J. W. Tester, W. G. Worley, B. A. Robinson, C. O. Grigsby, J. L. Feerer, *Geochim. Cosmochim. Acta* **1994**, 58, 2407.
- [78] J.-H. Park, L. Gu, G. von Maltzahn, E. Ruoslahti, S. N. Bhatia, M. J. Sailor, *Nat. Mater.* **2009**, 8, 331.
- [79] S. H. C. Anderson, H. Elliott, D. J. Wallis, L. T. Canham, J. J. Powell, *Phys. Status Solidi A* **2003**, 197, 331.